Thermo-Optic Measurements and their Inter-Dependencies for Delineating Cancerous Breast Biopsy Tissue from Adjacent Normal

Uttam M. Pal, Anil Vishnu GK, Manoj Varma, Jayant S. Vaidya, Hardik J. Pandya*

***Abstract*— The histopathological diagnosis of cancer is the current gold standard to differentiate normal from cancerous tissues. We propose a portable platform prototype to characterize the tissue's thermal and optical properties, and their inter-dependencies to potentially aid the pathologist in making an informed decision. The measurements were performed on samples from 10 samples from 5 subjects, where the cancerous and adjacent normal were extracted from the same patient. It was observed that thermal conductivity (k) and reduced-scattering-coefficient (μ'_s) for both the cancerous and normal tissues reduced with the rise in tissue temperature. Comparing cancerous and adjacent normal tissue, the difference in k and μ'_s (at 940nm) were statistically significant (p=7.94e-3), while combining k and μ'_s achieved the highest statistical significance (6.74e-4). These preliminary results promise and support testing on a large number of samples for rapidly differentiating cancerous from adjacent normal tissues.**

***Index Terms*— breast cancer, tissue diagnosis, portable system, Thermo-optic, Near-infrared, inverse optimization, thermal conductivity, reduced scattering coefficient.**

I. Introduction

BREAST cancer was responsible for 700,000 premature deaths worldwide in 2020 [1]. Current methods of diagnosis of breast cancer involve histopathological examination of the tissue. For this, the tissue needs to be first formalin-fixed, processed, and embedded in paraffin. Further processing involves using glass slides on which micrometer-thin tissue slices are mounted, stained using hematoxylin and eosin, and examined under the microscope by an experienced histopathology consultant doctor [2]. However, there is a critical need for a supplementary technique to perform a preliminary analysis of the ex-vivo biopsy sample in the operating room and provide immediate feedback over the adequacy of tumour resection. These additional techniques can potentially provide additional tissue attributes to support and aid the pathologist in making an informed decision.

Portable, low-cost systems have been proposed to provide cancer diagnostics in low-resource settings. Such techniques use different tissue properties to characterize various physiological conditions of the tissue under investigation. Micro-electromechanical system (MEMS) based devices have been proposed which characterize the thermal, mechanical, and electrical properties of the paraffin-embedded tissues [3]–[6]. However, MEMS-based probes are costly, and hence there is a critical need to develop an affordable tool to harness the bulk tissue properties.

The infrared thermography has been promising technique to detect breast cancer [7]–[11]. Bezerra et al. [8], [9] used a numerical method to solve an inverse problem to estimate the thermal properties on a numerical breast model. Figueiredo et al. [10] solved the inverse heat transfer numerical model and validated it using a silicone phantom tissue to localize the tumour regions. However, further studies to validate the thermal results on actual human breast tissues are required. With the advent of plug-in infrared (IR) cameras with the smartphone, instantaneous acquisition and data analysis of thermal images for biomedical applications have meant that if this approach is reliable, it could greatly aid quick diagnosis with a system that can be widely deployed worldwide, including low and middle income communities (LMIC) [12], [13].

Additionally, optical properties such as reduced scattering coefficient and absorption coefficient have also been explored for breast cancer diagnosis [14]–[18]. Pal et al. [14] and Spreinat et al. [18] proposed multispectral near-infrared techniques to diagnose breast and skin cancer, respectively. Jacques et al. [16] review the optical properties for different types of tissue. Depciuch et al. [17], [19] and Fernandez et al. [20] use commercial tools to quantify the optical properties of the paraffinized tissue using; however, such commercial tools are not designed to measure small tissue samples. Moreover, further studies need to be performed on the correlation between the thermal state of the tissue and the optical properties of the tissue.

There have been studies to quantify the temperature-dependent bulk optical properties using modified double integrating spheres [21]–[23]. Dressler et al. [21] performed the measurement on colon adenocarcinoma and breast adenocarcinoma tissue samples using sophisticated commercial

Uttam M. Pal and Anil Vishnu GK are with Department of Electronic Systems Engineering, the Indian Institute of Science, Bengaluru 560012, India.

Anil Vishnu GK is also with Center for BioSystems Science and Engineering, Indian Institute of Science.

Manoj Varma is with Centre for Nano Science and Engineering, Indian Institute of Science

Jayant S. Vaidya is with the Division of Surgery and Interventional Science, University College London, London WC1E 6BT, U.K.

Hardik J. Pandya is with the Department of Electronic Systems Engineering, the Indian Institute of Science, Bengaluru 560012, India (correspondence email: hjpandya@iisc.ac.in).

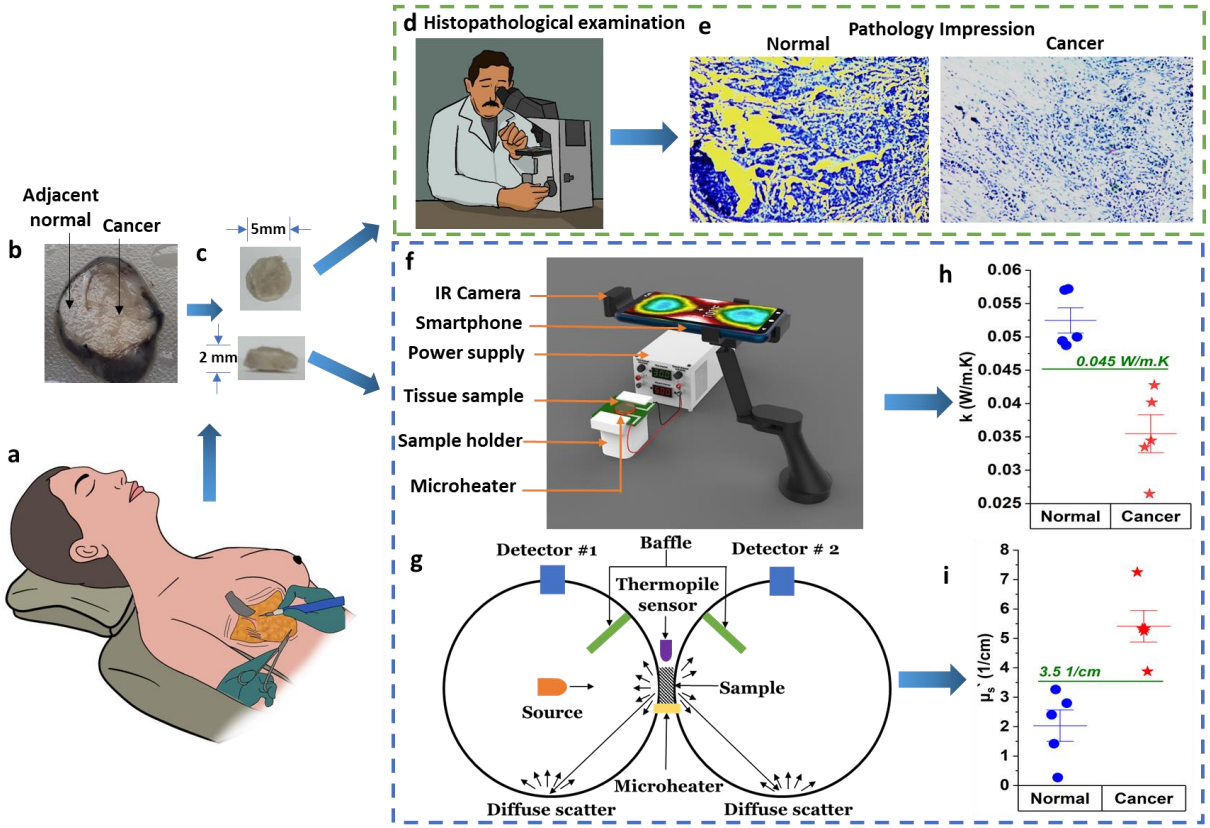

Fig. 1: Schematic representation of the histopathology test and the proposed assessment using thermo-optic properties of tissue. Experimental setup to measure the top surface temperature of sample tissue: a) Breast excisional surgery, b) Excised breast tissue with cancerous and adjacent normal, c) Uniform tissue core from the excised tissue using punch biopsy, d) Pathologist investigating the Hematoxylin and Eosin (H&E) stain slides, e) Histopathology image for cancer and normal tissue. Schematic of the experimental setup to measure, (f) thermal properties, and (g) Thermo-optic properties of the tissue sample. Panels h) and i) show the results of this study: h) Thermal conductivity and i) reduced scattering coefficient results.

instrumentations. Kara et al. [22] measured on a tissue phantom comprising of lipid emulsion with the tissue heated using Peltier units (i.e. hot plate). The instantaneous temperature monitoring was performed using CMOS sensors. Kim et al. [23] measured using porcine skin through heating a closed box using a heating gun, while using a thermocouple to monitor the temperature. However, more studies need to be performed for breast cancer diagnosis.

We proposed a heat source located within a cost-effective double integrating sphere and a non-contact temperature monitoring system to increase the product lifespan. Further studies were performed to quantify the temperature dependent optical properties and to define the cutoffs for the pathological human breast tissues.

This study reports the design and development of portable, affordable, and non-ionizing based mid-infrared thermal imaging and NIR (near-infrared) spectroscopy techniques to accurately delineate cancerous tissues from adjacent normal by characterizing the thermo-optic properties and their inter-dependencies.

II. Design And Methodology

This section describes the sample preparation and experimental setup to estimate the thermal conductivity and specific heat capacity using infrared imaging. We then discuss the modified double integrating spheres experimental setup to evaluate the temperature-dependent bulk optical properties.

A. Sample Preparation

As shown in Fig. 1a-b, the suspected cancerous lesions along with the adjacent normal tissues are removed by the surgeon during the breast excision surgery. These excised tissues are then fixed with 10% buffered formalin solution by the oncopathologist for further processing and routine examination. The samples required for performing the study were then extracted from these formalin-fixed excised specimens by the consultant oncopathologist using a core biopsy needle to get uniform biopsy tissue samples (diameter of 5 mm and thickness of 2 mm) as shown in Fig. 1c. The biopsy tissue samples were identified as cancerous or adjacent normal by the oncopathologist using the immunohistopathology tests through hematoxylin and eosin staining, as shown in Fig. 1e. The biopsy tissues were collected from N = 5 subjects (n = 5 are Invasive Ductal Carcinoma (IDC), and n = 5 are adjacent normal). The standard deviation of the tissue thickness and diameter are ±0.063 mm and ±0.032 mm, respectively. The samples were then stored in buffered formalin in 1.5 mL tubes for measurements. Even though formalin-fixed, the samples are reported to preserve the main tissue constituents such as lipids and collagen [24], [25]. All the studies were performed in accordance with the institutional ethics committee of Assam Medical College and the Indian Institute of Science with the

ethical clearance certificate number AM/EC/1333 and 17-14012020, respectively.

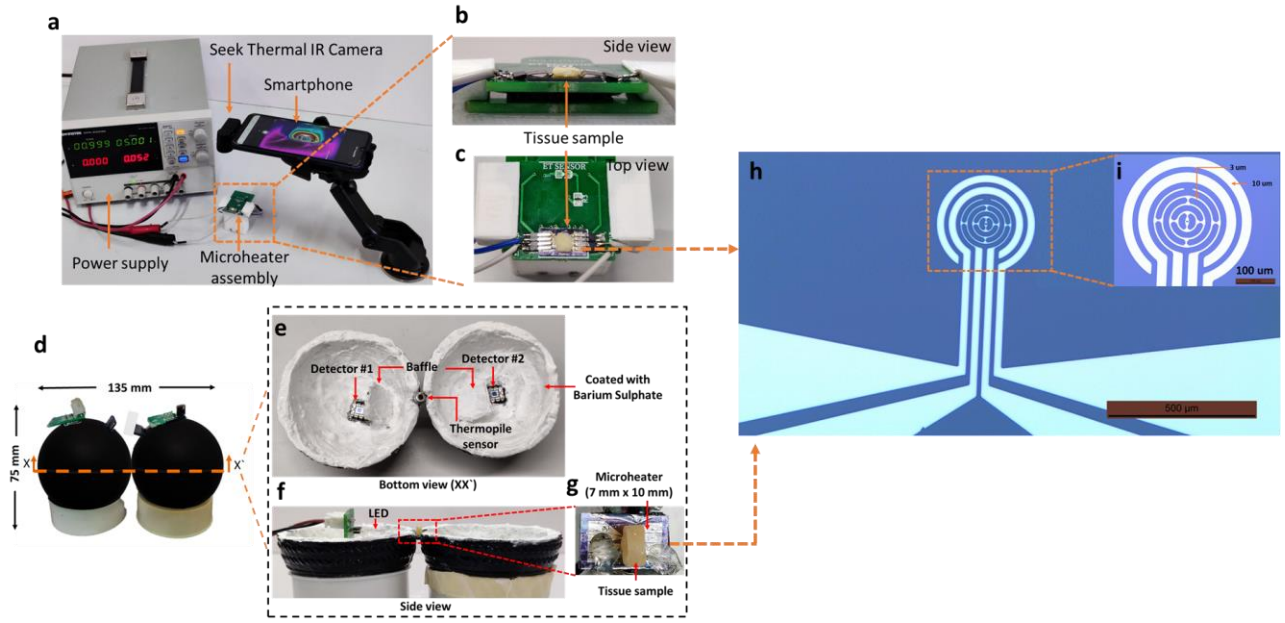

Fig. 2: Experimental setup to measure the thermal and thermo-optic properties of the tissue. a) Experimental setup to measure the thermal properties of the breast tissue. b) Side view and c) Top view of the microheater. d) Experimental setup of the modified double integrating sphere to study the temperature effect on the optical properties of tissues, e) Bottom view showcasing the detectors, baffle, and thermopile sensor, f) Side view showcasing the source LED operating at 940 nm, sample tissue, and microheater, g) Zoom top view of the microheater along with the sample tissue. h) SEM image of the microheater along with i) Zoom view of the microheater with dimension.

B. Microheater Fabrication

The microheater was fabricated on a silicon substrate as a microchip using a single mask process. Platinum was used as the material to create the microheater. The microchip consists of the microheater and a pair of electrodes for characterizing the electrical properties of the platinum film that was deposited. A standard 4-inch silicon wafer was first oxidized to create 1 µm thick oxide layer. MICROPOSIT S1813 Photoresist was spin-coated on the oxidized wafer and patterned through photolithography using MJB4 mask aligner system. The patterning is performed using a photomask that has the microheater's design, and characterization electrodes patterned on it. After development and hard baking, titanium/platinum of thickness 25 nm/190 nm was deposited on the oxidized silicon wafer using Tecport E-beam evaporator. A lift-off process using acetone and isopropanol (IPA) patterns the deposited Ti/Pt layer to create the wafer's microheater structure. The individual microchips that contain the microheaters and characterization electrodes are then diced and separated from the 4-inch wafer using an automatic dicing machine as shown in Fig. 2h-i.

C. Experimental Setup to Estimate the Thermal Properties of the Breast Tissue

The schematic of the placement of the tissue samples on the microheater assembly as shown in the Fig. 1f. The experimental setup is shown in Fig. 2a-c. The infrared camera (Seek Thermal Compact Pro), which includes an array of thermopile sensors was placed above the microheater assembly. The infrared camera with its C-type USB attachment was connected to the smartphone and the thermal image was captured using Seek Thermal android application. The camera has a resolution of 320 x 240 pixels with a 32° field of view and measures infrared spectrum from 7.5 µm to 14 µm, while drawing a minimal 280 mW of power from the smartphone. The IR camera was placed 10 cm above the microheater assembly from the sample tissue as mentioned in the specification sheet of the camera, while the zoom feature of IR camera was used to improve the resolution of the image. The white cross marker feature in the smartphone app was aligned over the center of the tissue to measure the temperature of the tissue.

The microheater locally heats the tissue samples from the bottom surface, while the thermal image from the top surface is captured using the infrared camera. The microheater is designed in a way such that the tissue heating is uniform within the area covered by the heating element. The microheater is made to have a full contact with the tissue's bottom surface to ensure appropriate heat conduction leading to uniform heating throughout the tissue samples as shown in Fig. 2 b-c. The resistance of the platinum microheater at zero heating was measured to be 121±3 Ω.

Once the microheater's temperature was calibrated, the voltage was applied across the microheater, and the top surface temperature was measured using the IR camera. The input voltage was parametrically swept from 0 V to 8 V with a step of 0.5 V, with each voltage applied for 2 mins to stabilize the temperature (30°C to 50°C) within the sample tissue. The microheater temperature was calibrated with respect to the applied voltage, as shown in Fig. 3a, along with the error. The tissue top surface temperature and the error band representing the standard deviation with respect to the applied bottom

surface temperature are shown in Fig. 3b. As the standard deviation of the sample tissue thickness is ±0.063 mm, errors due to the difference in the tissue's thermal behavior as a function of the difference in thickness performed using FEM tool were found to be negligible (~0.4%) and hence neglected. All the measurements were performed in the class 10000 cleanroom lab with a controlled ambient temperature of 25 ±1 °C

It can be observed that raw infrared images can directly differentiate the cancerous from adjacent normal breast biopsy tissue. However, the absolute values of bulk thermal properties (thermal conductivity and specific heat capacity), and bulk optical properties (reduced scattering coefficient and absorption coefficient) are well documented and referenced for the cancerous and normal tissues [16], [26], [27]. Hence the quantification of the bulk thermal and optical properties adds more value to the information available with the pathologist to differentiate cancerous tissue from adjacent normal as described in the next section.

D. Thermal Properties of the Tissue and Inverse Optimization Problem

The heat transmission through the tissue sample can be expressed using the Poisson's equation assuming the steady-state conditions [28], [29].

$$Q = k\nabla^2 T \tag{1}$$

where k is the thermal conductivity (W/m.K), Q is the amount of heat supplied (W/m^3), and T is the temperature. In the case of transient conditions, the time-dependent temperature can be defined using the heat equations[28], [29].

$$\frac{\partial T}{\partial t} = \left(\frac{k}{\rho . C_p}\right)\nabla^2 T \tag{2}$$

where C_p is the specific heat capacity (J/Kg.K) and ρ is the density (Kg/m^3).

The cylindrical tissue samples placed above the microheater were assumed to undergo uniform heating. Under such an assumption, the thermal conductivity and specific heat capacity can be analytically evaluated with the time-dependent top and bottom surface temperature of tissues.

$$k = \left(\frac{Qd}{A\Delta T_s}\right) \tag{3}$$

$$\mathrm{Q} = \mathrm{m}C_p\Delta T_t \tag{4}$$

where Q is the quantity of heat transferred, d is the thickness of the tissue, A is the cross-sectional area, $\Delta T_s = T_{bottom} - T_{top}$, where the T_{bottom} and T_{top} is the bottom and top surface temperature respectively. For the specific heat capacity (C_p), m is the mass of the tissue and ΔT_t is the change in temperature at the top surface of the tissue with respect to a specified time step. However, the analytic expression does not account for the convective heat flux for the adjacent surfaces of the sample tissues. Hence, the inverse optimization problem was solved using the heat transfer numerical model (FEM) using COMSOL Multiphysics to estimate the values of thermal conductivity and specific heat [30]. It can be observed from Eqn. 3 that the value of thermal conductivity can be estimated following steady-state values of tissue temperature, while the estimation of specific

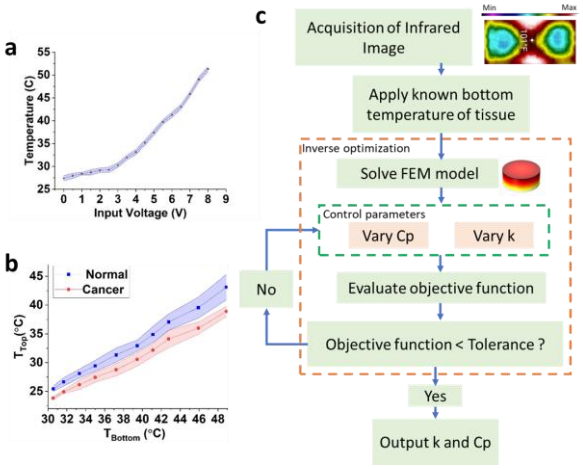

Fig. 3: a) The calibrated temperature with respect to applied voltage, b) Temperature at the top surface of the tissue with respect to the calibrated bottom surface temperature, and c) The inverse optimization algorithm used to estimate the thermal properties of the breast tissue samples.

heat capacity requires the transient value of tissue temperature. The inherent nature of the analysis (stationary and transient) can be utilized to setup two different types of optimization problems. A stationary optimization problem can be set to quantify the temperature-dependent thermal conductivity. While the transient optimization could be setup to estimate the averaged thermal conductivity and specific heat capacity, as shown in the Fig. 3c.

The inverse optimization algorithm involves taking the infrared image. A white cross marker aligned at the center of the tissue is used to measure the top surface temperature of the tissue. Two set of inverse optimizations were performed to quantify the thermal properties. The first steady-state inverse problem was solved to quantify the temperature-dependent thermal conductivity by minimizing the steady-state objective function as shown in Eqn. 5. The first objective function took account of the steady-state experimental temperature (T_e) and computed temperature (T_c) using the FEM model. The FEM model for the first inverse problem involves setting up a cylindrical geometry of 5 mm diameter and 2mm thickness. The temperature boundary condition was applied at the bottom of the cylinder, and the temperature was swept from 30 °C to 50 °C. The stationary study, along with the optimization, was solved to minimize the objective function till the averaged top surface temperature matches the experimental value. The optimization problem hence estimates for thermal conductivity as a function of applied temperature.

The second inverse problem minimized the transient objective function to quantify the average thermal conductivity (k) and specific heat capacity (C_p) as shown in Eqn. 6. This inverse problem involved defining a time-dependent objective function that integrates the square of the difference between the time-dependent experimental temperature ($T\_e\,(t)$) and time-dependent computed temperature (($T\_c\,(t)$) using the FEM model. The upper and lower bound for k was used as 0.1 W/m.K and 0.6 W/m.K, while for C_p as 3400 J/Kg.K and 3800 J/Kg.K respectively. The values of the upper and lower bounds were

assumed based on the literature survey [31], [32]. In both the cases, the Nelder-Mead optimization algorithm was used to minimize the objective function.

$$\text{Objective function (Steady state)} = \left(\frac{T_e - T_c}{T_e}\right)^2 \quad (5)$$

$$\text{Objective function (Transient)} = \int_0^T \left(\frac{T_e(t) - T_c(t)}{T_e(t)}\right)^2 \quad (6)$$

subject to

$k^L < k < k^U$

$Cp^L < Cp < Cp^U$

where k^L, k^U and Cp^L, Cp^U are the lower and upper bounds of the control parameter k and Cp, respectively.

E. Experimental Setup to Measure the Temperature dependent Bulk Optical Properties

The double integrating sphere was modified to include the microheater and a single thermopile sensor to study the temperature effect on the bulk optical properties such as reduced scattering coefficient and absorption coefficient using near-infrared spectroscopy. The double integrating sphere's inner surface was coated with Barium Sulphate to have a very high reflectance (~ 98%). The OFL-5102 LED from Multicomp with a peak operating wavelength of 940 nm was used to perform the NIR spectroscopy measurements. The operating wavelength of 940 nm was selected because the optical reduced scattering coefficient at 940 nm could significantly distinguish between cancer and normal tissues in our earlier work [14]. The narrow beamwidth (~10°) of the LED along with the Fresnel lens focused the light at the center of the tissue sample. The double integrating sphere's baffle restricted the direct light scattered from the tissue sample towards the optical detector. The silicon-based OPT101 from Texas Instrument was used to quantify the back-scattered and forward-scattered light. The OPT101 with silicon photodiode detector along with on-chip transimpedance amplifier adds the ease-of-use and robustness for the long run of the instrumentation. The detector had a wide range of sensitivity spread over the visible and near-infrared spectrum. More than 50% sensitivity was observed between 550 nm and 1000 nm, while at the operating wavelength of 940 nm, the detector was 85% sensitive.

The schematic of the instrumentation involving the double integrating sphere is shown in Fig. 1g. The double integrating sphere was designed and developed by performing a horizontal incision on two spherical rubber balls, as shown in Fig. 2d-g. The overall dimension of the double integrating sphere setup was measured as 135 mm x 75 mm. The LED was placed at the center of the first integrating sphere to focus the light at the center of the tissue. Further incisions were made to incorporate the microheater at the bottom conjunction of the two-integrating sphere, as shown in Fig. 2e-f. Another incision was made to adjust the thermopile sensor at the top conjunction of the two-integrating sphere, as shown in Fig. 2e. The thermopile is a point infrared sensor ZTP-135SR from Amphenol Advanced Sensors and was used to measure the tissue temperature that was locally heated using the microheater beneath, as shown in Fig. 2 f-g. The overall dimension of the microchip integrating a microheater was 7 mm x 12 mm, while the diameter of the active area of the microheater was 340 µm.

TABLE I
THERMO-OPTIC SYSTEM SPECIFICATION

Requirements	Specification
Power supply	230 V (50 Hz)
Thermal operation	Quasi-Stationary
Thermal source	Microheater (121±3 Ω)
Thermal detector	Seek Thermal Compact Pro and ZTP-135SR thermopile sensor
Optical operation	Continuous wave (CW)
Operating wavelength	940 nm
Optical source	Narrow beamwidth and narrow bandwidth LED
Optical detector	Si PD with integrated amplifier (OPT101)
Portable	Yes
Tissue sample dimension	5 mm diameter and 2 mm thickness
Tissue type	Formalin-Fixed tissue samples
Approximate cost of the prototype	$500

The feature size of the platinum microheater is 3um, as shown in Fig. 2i. The infrared sensor was selected to have a low field of view (~80°) to locally measure the surface temperature of the tissue. The output voltage from the ZTP-135SR with respect to the incident temperature was first calibrated before embedding inside the double integrating sphere. The sample tissue in this configuration was arranged in a standing position (longitudinal) over the microheater to enable transverse incidence of the light beam at the center of the tissue.

The diffused reflectance (M_R) and transmittance (M_T) were measured using the detector #1 and detector #2 respectively as shown in the Eqn. 7 and 8.

$$M_R = \frac{R(r,r,t,t) - R(0,0,0,0)}{R(r,r,0,0) - R(0,0,0,0)} \quad (7)$$

$$M_T = \frac{T(r,r,t,t) - T(0,0,0,0)}{T(0,0,1,1) - T(0,0,0,0)} \quad (8)$$

where *R(r,r,t,t)* and *T(r,r,t,t)* are the measured voltage by detector #1 and detector #2 respectively, as shown in Fig. 2e when the source is switched ON. *R(0,0,0,0)* is the measured voltage by detector #1 when the sample at the exit port of the first integrating sphere is removed. *R(r,r,0,0)* is the measured voltage by detector #1 when a reflectance standard ($BaSO_4$) is placed at the exit port of the first integrating sphere. *T(0,0,1,1)* is the measured voltage by detector #2 when the sample is removed from the double integrating sphere. *T(0,0,0,0)* is the measured voltage by detector #2 when the source LED was switched OFF.

The Inverse Adding-Doubling (IAD) code which performs a Monte Carlo (MC) simulation to model the diffused nature of photons, was used to quantify the bulk optical properties from the measured M_R and M_T [33]. The IAD code required different parameters of the double integrating sphere, such as sphere diameter, percentage reflectance of the inner coating material (~98%), number of spheres, the thickness of the sample, and the illumination beam diameter as input parameters. The full specification of the prototype system is summarized in Table I.

III. Results And Discussions

The thermal and optical measurements were performed for three times for each sample, and the mean results with standard deviation are reported.

A. Thermal Properties of the Breast Tissue Samples

Solving the first steady-state inverse optimization problem gives the estimation of the temperature dependent thermal conductivity as shown in Fig. 4a. The normal tissues are observed to have higher thermal conductivity as compared to the cancerous tissues. It is also observed that the thermal conductivity for both the cancerous and the adjacent normal tissues tends to increase with the rise of applied temperature. The difference in thermal conductivity for the cancerous and adjacent normal tissues is statistically significant (p=0.00794). The non-parametric Mann Whitney U test was performed to calculate the statistical significance.

The second optimization problem solved time dependent objective function for the average thermal conductivity and specific heat capacity. The average thermal conductivity for the cancerous and normal tissues are reported as 0.0354 (±0.0063) W/m.K and 0.0524 (±0.0042) W/m.K, respectively. Moreover, the average specific heat capacity for the cancerous and normal tissues are reported as 3618.26 (±31.89) J/Kg.K and 3584.76 (±32.44) J/Kg.K respectively. The transfer of heat energy from the bottom surface to the top surface of the tissue is observed to be quicker in the case of normal compared to cancerous tissue, which can be deduced from the reported higher thermal conductivity for adjacent normal tissue compared to cancer. The difference in the average thermal conductivity between the cancerous tissue and adjacent normal is reported to be statistically significant (p=0.00794). Even though the average specific heat capacity of the cancer tissue is reported to be higher than normal tissues, it is not statistically significant (p=0.1507). The cutoff for thermal conductivity was observed as 0.45 W/m.K. The measured thermal conductivity and specific heat capacity for each of the tissue samples are reported in Table II.

B. Temperature dependent Bulk Optical Properties of the Breast Tissue Samples

The reduced scattering coefficient ($\mu`_s$) at the operating wavelength of 940 nm is observed to be significantly higher in cancerous tissues as compared to normal tissues, a basis for delineation. As the temperature of the tissues is increased from 23 °C to 42 °C, a slight decrease in $\mu`_s$ is observed for both the cancerous and normal tissues as shown in Fig. 5. The cut-off is also observed to reduce with the rise in tissue temperature with the value of 3.5 1/cm at 37.5 °C. Using the curve-fitting, the relation between the $\mu`_s$ and the operating temperature (T) at the operating wavelength of 940 nm can be evaluated with a quadratic function as shown in Eq. 9 and 10.

$$\mu`_{sc} = -(1.9 \times 10^{-4})T^2 + (89 \times 10^{-4})T + 0.47 \quad (9)$$

$$\mu`_{sc} = -(5 \times 10^{-5})T^2 + (8.7 \times 10^{-4})T + 0.24 \quad (10)$$

where $\mu`_{sc}$ and $\mu`_{sn}$ are the reduced scattering coefficient for cancerous and normal tissues, respectively. It is also observed

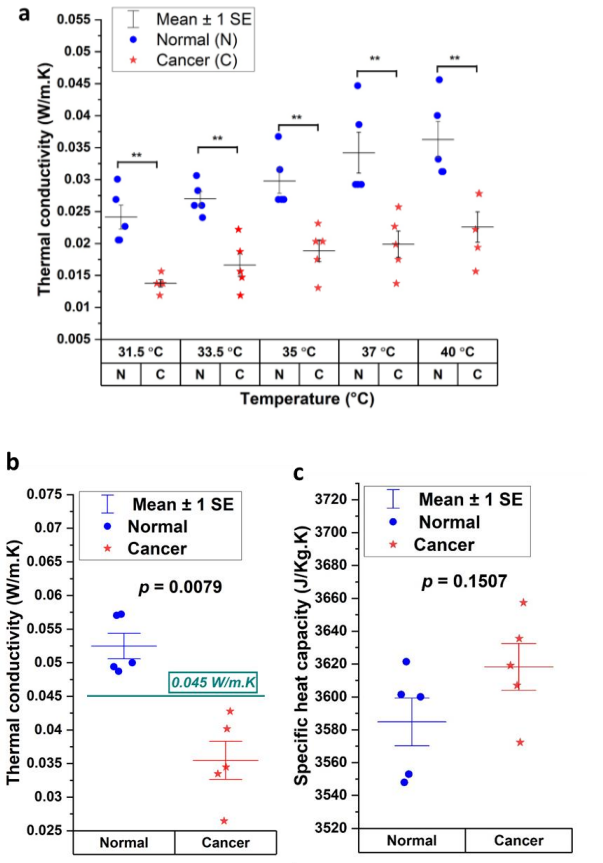

Fig. 4: a) Thermal conductivity of the normal and cancerous formalin-fixed tissues as a function of tissue's bottom surface temperature. Comparison of the computed b) Averaged thermal conductivity (k) and c) Averaged specific heat capacity (Cp) for the normal and cancerous formalin-fixed tissues by performing the multi-parameter transient inverse optimization.

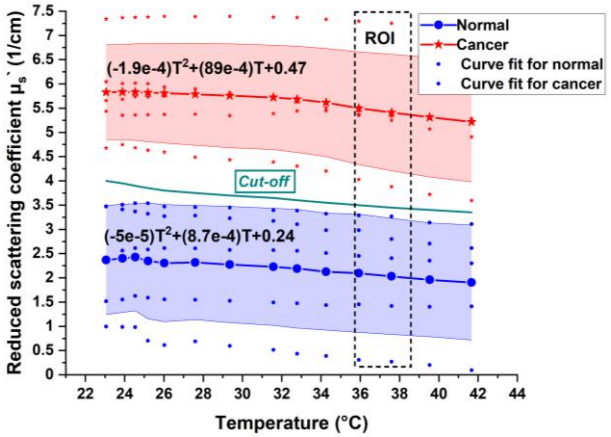

Fig. 5: Reduced scattering coefficient ($\mu`_s$) measured as a function of temperature. The measurement was performed at the operating wavelength of 940 nm. The mean values of the normal and cancer were curve fitted to a quadratic equation.

that the $\mu`_{sc}$ reduces with higher slope values as compared to $\mu`_{sn}$, especially within the region of interest (ROI) between 36 °C and 38.5 °C, an additional basis for delineation. The slope can be of interest specifically if the overlapping values of $\mu`_s$ are observed for both the normal and cancerous tissues, as seen

TABLE II

BULK THERMAL AND OPTICAL PROPERTIES FOR FORMALIN-FIXED TISSUES

SN	k (W/m.K)		C_p (J/Kg.K)		μ'_s (1/cm) @ 940 nm and 37.5°C	
	N	C	N	C	N	C
1	0.057	0.040	3548	3572.3	1.419	5.339
2	0.057	0.026	3553	3607	0.2684	5.334
3	0.048	0.033	3621.4	3619.1	3.265	7.25
4	0.05	0.034	3600	3635.5	2.799	5.248
5	0.049	0.042	3601.4	3657.4	2.403	3.878
Avg.	**0.052**	**0.035**	**3584.76**	**3618.26**	**2.03088**	**5.4098**
STD	**0.0042**	**0.0063**	**32.44**	**31.89**	**1.19**	**1.20**

where,
k – Thermal conductivity (W/m.K)
C_p – Specific heat capacity (J/Kg.K)
μ'_s – Optical reduced scattering coefficient (1/cm) at 37.5 °C
N – Normal and C – Cancer.

TABLE III

STATISTICAL ANALYSIS FOR DIFFERENT EVALUATED PARAMETERS

Parameters	p-value	Significance
k	7.94e-3	****
Cp	1.507e-1	ns
μ'_s	7.94e-3	**
k and Cp	9.25e-3	**
k and μ'_s	6.74e-4	***
K, Cp, and μ'_s	7.55e-4	***

in Fig 5. The difference in reduced scattering coefficient between the cancerous and adjacent normal tissues within the region of interest (ROI) are statistically significant (p=0.00794). The absorption coefficient (μ_a) at 37.5 °C for the cancerous and adjacent normal tissues are reported as 1.81 (±1.37) 1/cm and 1.12 (±1.16) 1/cm respectively, but not statistically significant (p=0.420). The reduced optical scattering coefficient for each of the tissue sample is reported in Table II.

C. Discussion on the Combined Thermo-optic Results

Differentiating the normal and cancer tissue based on only specific heat capacity is observed to be statistically insignificant (p = 0.1507). However, when the results form specific heat capacity is combined with the thermal conductivity, the result is statistically significant (p = 0.00925). The Fisher's combined probability test is used to perform a combined p-value over the independent tests. When the outcomes from thermal conductivity and reduced optical scattering are combined, the results are distinctly statistically significant (p = 0.000674). When all the three parameters (k, Cp, and μ'_s) are combined, the result is statistically significant (p = 0.000755). The p-value for each of the individual and the combined tests are tabulated in Table III.

D. Discussion on the Physiology of the Cancer and Normal Tissues

The reason behind the lower k value in cancerous tissue compared to normal tissues could possibly be the increase in collagen (structural protein) in cancer cells which have thermal conductivity between 0.2 and 0.3 W/m.K [34]. Even though the tissue is formalin-fixed, the tissue still preserves the tissue constituents such as lipids and collagen [24], [25]. Higher specific heat capacity has been reported in cancerous compared to normal tissues [32], [35], the possible reason being higher lipid content in normal compared to cancer, because the lipids (structurally fats) has lower specific heat.

Higher scattering is observed in cancerous tissues due to multiple gradients and discontinuities of refractive index observed as the light propagates through the tissue. This behavior is because of the presence of high fibrous content in cancerous tissue [36], [37]. Additionally, with the rise of tissue temperature, the tissue volume increases, reducing the density of scatters within the tissue. This results in the dip of the reduced scattering coefficient for both the normal and cancer tissues as the temperature increases [22], [23].

E. Limitations of the Current Study and Future Work

The fresh tissues were formalin-fixed before performing the thermal and optical measurements, which may deprive it of the original tissue properties. In this proof-of-principle study, the number of samples was small, and the measurements were carried out on tissues from just five subjects. Yet, the technique appears to yield a high level of accuracy in discerning cancer from normal tissues, particularly by combining two physical properties. The accuracy of the test needs to be validated on a larger number of samples. This will help us arrive at sensitivity and specificity values for the proposed dual modality.
In the future work, we envisage the study of bulk optical and thermal properties parameters at the interface of normal and cancerous tissue and perform further experiments on extensive numbers of fresh breast tissue samples.

IV. COST ANALYSIS

The entire cost of the platform including the IR Seek Thermal Compact pro cameras, thermopile sensor, source LED, optical detector, microchip fabrication, display system, and electronic components amounts to around $500. The maintenance cost would be $10 per sample. When produced at an industrial scale, these costs should be lower.

V. CONCLUSION

In this paper, we discuss the design and implementation of a portable tool that characterizes the bulk thermal and optical properties of the tissue. With regards to thermal properties, the bulk thermal conductivity (k) proved to be the critical thermal parameter that could differentiate the cancerous from normal tissues. The reduced scattering coefficient (μ'_s) operated at 940 nm proved to be the critical optical tissue parameter that can delineate cancerous from normal tissues. However, combining both the critical parameters (k and μ'_s) gave the highest accuracy for delineating cancer from normal tissues.

This novel thermo-optic tool can rapidly differentiate cancerous from adjacent normal breast biopsy tissues and aid the pathologist to make an immediate feedback in the operating room.

VI. AUTHORS' CONTRIBUTIONS

Conceptualization: UP and HJP
Tool design and fabrication: UP, AV, and HJP
Experiments: UP, AV, and HJP
Analysis: UP, MV, JSV, and HJP
Interpretation: UP, MV, and HJP
Funding acquisition: HJP

Investigation: UP, MV, JSV, and HJP
Methodology: UP and HJP
Project Administration: HJP
Supervision: HJP
Validation: UP, MV, and HJP
Visualization: UP, AV, and HJP
Manuscript Preparation: UP, AV, MV, JSV, and HJP

VII. ACKNOWLEDGEMENT

Uttam M. Pal acknowledges Dr. Vineet Dravid for helping in data analysis and Dr. Arup Polly for research insights and feedback on experimental protocols. Uttam M. Pal also acknowledges Ashika Nayak, Tejaswi Medisetti for helping with the data analysis. Arpita Sarkar and Adithya Kumar are acknowledged for their help in preparing Figure 1. Hardik J. Pandya acknowledges Tata Trusts for the short-term travel grant which resulted in collaboration with Jayant S. Vaidya, University College London.

VIII. CONFLICT OF INTEREST

The authors declare no financial or commercial conflict of interest.

IX. REFERENCES

[1] "Global cancer observatory," 2020. https://gco.iarc.fr/ (accessed Dec. 16, 2020).

[2] G. Balasundaram *et al.*, "Biophotonic technologies for assessment of breast tumor surgical margins—A review," *J. Biophotonics*, vol. 14, no. 1, p. e202000280, Jan. 2021, doi: 10.1002/jbio.202000280.

[3] H. J. Pandya, K. Park, W. Chen, L. A. Goodell, D. J. Foran, and J. P. Desai, "Toward a Portable Cancer Diagnostic Tool Using a Disposable MEMS-Based Biochip," *IEEE Trans. Biomed. Eng.*, vol. 63, no. 7, pp. 1347–1353, Jul. 2016, doi: 10.1109/TBME.2016.2535364.

[4] H. J. Pandya, K. Park, and J. P. Desai, "Design and fabrication of a flexible MEMS-based electro-mechanical sensor array for breast cancer diagnosis," *J. Micromechanics Microengineering*, vol. 25, no. 7, Jul. 2015, doi: 10.1088/0960-1317/25/7/075025.

[5] H. J. Pandya, W. Chen, L. A. Goodell, D. J. Foran, and J. P. Desai, "Mechanical phenotyping of breast cancer using MEMS: A method to demarcate benign and cancerous breast tissues," *Lab Chip*, vol. 14, no. 23, pp. 4523–4532, Dec. 2014, doi: 10.1039/c4lc00594e.

[6] H. J. Pandya *et al.*, "Towards an automated MEMS-based characterization of benign and cancerous breast tissue using bioimpedance measurements," *Sensors Actuators, B Chem.*, vol. 199, pp. 259–268, 2014, doi: 10.1016/j.snb.2014.03.065.

[7] J. L. Gonzalez-Hernandez, A. N. Recinella, S. G. Kandlikar, D. Dabydeen, L. Medeiros, and P. Phatak, "Technology, application and potential of dynamic breast thermography for the detection of breast cancer," *International Journal of Heat and Mass Transfer*, vol. 131. Elsevier Ltd, pp. 558–573, Mar. 01, 2019, doi: 10.1016/j.ijheatmasstransfer.2018.11.089.

[8] L. A. Bezerra *et al.*, "Estimation of breast tumor thermal properties using infrared images," *Signal Processing*, vol. 93, no. 10, pp. 2851–2863, 2013, doi: 10.1016/j.sigpro.2012.06.002.

[9] L. A. Bezerra, R. R. Ribeiro, P. R. M. Lyra, and R. C. F. Lima, "An empirical correlation to estimate thermal properties of the breast and of the breast nodule using thermographic images and optimization techniques," *Int. J. Heat Mass Transf.*, vol. 149, 2020, doi: 10.1016/j.ijheatmasstransfer.2019.119215.

[10] A. A. A. Figueiredo, H. C. Fernandes, and G. Guimaraes, "Experimental approach for breast cancer center estimation using infrared thermography," *Infrared Phys. Technol.*, vol. 95, pp. 100–112, Dec. 2018, doi: 10.1016/j.infrared.2018.10.027.

[11] C. Song, C. A. Purdie, S. I. Brown, T. Frank, and J. S. Vaidya, "Dynamic response to heat - A novel physical characteristic of breast cancer," *Int. J. Surg.*, vol. 6, no. 4, pp. 357–358, 2008, doi: 10.1016/j.ijsu.2008.02.002.

[12] A. Kirimtat, O. Krejcar, and A. Selamat, "A Mini-review of Biomedical Infrared Thermography (B-IRT)," in *Lecture Notes in Computer Science (including subseries Lecture Notes in Artificial Intelligence and Lecture Notes in Bioinformatics)*, May 2019, vol. 11466 LNBI, pp. 99–110, doi: 10.1007/978-3-030-17935-9_10.

[13] A. Kirimtat, O. Krejcar, A. Selamat, and E. Herrera-Viedma, "FLIR vs SEEK thermal cameras in biomedicine: Comparative diagnosis through infrared thermography," *BMC Bioinformatics*, vol. 21, no. S2, p. 88, Mar. 2020, doi: 10.1186/s12859-020-3355-7.

[14] U. M. Pal *et al.*, "Towards a Portable Platform Integrated with Multispectral Noncontact Probes for Delineating Normal and Breast Cancer Tissue Based on Near-Infrared Spectroscopy," *IEEE Trans. Biomed. Circuits Syst.*, vol. 14, no. 4, pp. 879–888, Aug. 2020, doi: 10.1109/TBCAS.2020.3005971.

[15] U. M. Pal *et al.*, "Optical spectroscopy-based imaging techniques for the diagnosis of breast cancer: A novel approach," *Appl. Spectrosc. Rev.*, vol. 55, no. 8, 2020, doi: 10.1080/05704928.2020.1749651.

[16] S. L. Jacques, "Optical properties of biological tissues: A review," *Phys. Med. Biol.*, vol. 58, no. 11, 2013, doi: 10.1088/0031-9155/58/11/R37.

[17] J. Depciuch *et al.*, "Comparing paraffined and deparaffinized breast cancer tissue samples and an analysis of Raman spectroscopy and infrared methods," *Infrared Phys. Technol.*, vol. 76, no. May 2018, pp. 217–226, 2016, doi: 10.1016/j.infrared.2016.02.006.

[18] A. Spreinat, G. Selvaggio, L. Erpenbeck, and S. Kruss, "Multispectral near infrared absorption imaging for histology of skin cancer," *J. Biophotonics*, vol. 13, no. 1, p. e201960080, Jan. 2020, doi: 10.1002/jbio.201960080.

[19] J. Depciuch *et al.*, "Monitoring breast cancer treatment

using a Fourier transform infrared spectroscopy-based computational model," *J. Pharm. Biomed. Anal.*, vol. 143, pp. 261–268, Sep. 2017, doi: 10.1016/j.jpba.2017.04.039.

[20] D. C. Fernandez, R. Bhargava, S. M. Hewitt, and I. W. Levin, "Infrared spectroscopic imaging for histopathologic recognition," *Nat. Biotechnol.*, vol. 23, no. 4, pp. 469–474, 2005, doi: 10.1038/nbt1080.

[21] C. Dressler, D. Schwandt, J. Beuthan, V. Mildaziene, U. Zabarylo, and O. Minet, "Thermally induced changes of optical and vital parameters in human cancer cells," *Laser Phys. Lett.*, vol. 7, no. 11, pp. 817–823, Nov. 2010, doi: 10.1002/lapl.201010070.

[22] E. Kara, İ. Çilesiz, and M. Gülsoy, "Monitoring system for investigating the effect of temperature change on optical properties," *Lasers Med. Sci.*, vol. 33, no. 8, pp. 1763–1768, Nov. 2018, doi: 10.1007/s10103-018-2537-2.

[23] S. Kim and S. Jeong, "Effects of temperature-dependent optical properties on the fluence rate and temperature of biological tissue during low-level laser therapy," *Lasers Med. Sci.*, vol. 29, no. 2, pp. 637–644, Jun. 2014, doi: 10.1007/s10103-013-1376-4.

[24] H. J. Butler *et al.*, "Shining a light on clinical spectroscopy: Translation of diagnostic IR, 2D-IR and Raman spectroscopy towards the clinic," *Clin. Spectrosc.*, vol. 1, p. 100003, Dec. 2019, doi: 10.1016/j.clispe.2020.100003.

[25] S. Kumar, A. Srinivasan, and F. Nikolajeff, "Role of Infrared Spectroscopy and Imaging in Cancer Diagnosis," *Curr. Med. Chem.*, vol. 25, no. 9, pp. 1055–1072, 2018, doi: 10.2174/0929867324666170523121314.

[26] J. C. Bamber and C. R. Hill, "Acoustic properties of normal and cancerous human liver-I. Dependence on pathological condition," *Ultrasound Med. Biol.*, vol. 7, no. 2, pp. 121–133, 1981, doi: 10.1016/0301-5629(81)90001-6.

[27] O. Abdel Alim, M. M. Mohamed, and L. Shaat, "Modeling the acoustic attenuation process of soft tissues," *J. Phys.*, vol. 4, no. 5 pt 2, pp. 1263–1266, 1994, doi: 10.1051/jp4:19945280.

[28] C. Rossmanna and D. Haemmerich, "Review of temperature dependence of thermal properties, dielectric properties, and perfusion of biological tissues at hyperthermic and ablation temperatures," *Crit. Rev. Biomed. Eng.*, vol. 42, no. 6, pp. 467–492, Jun. 2014, doi: 10.1615/CritRevBiomedEng.2015012486.

[29] D. Haemmerich, D. J. Schutt, I. Dos Santos, J. G. Webster, and D. M. Mahvi, "Measurement of temperature-dependent specific heat of biological tissues," *Physiol. Meas.*, vol. 26, no. 1, pp. 59–67, 2005, doi: 10.1088/0967-3334/26/1/006.

[30] "COMSOL Multiphysics® Modeling Software." https://www.comsol.com/.

[31] N. P. Silva, A. Bottiglieri, R. C. Conceição, M. O'halloran, and L. Farina, "Characterisation of ex vivo liver thermal properties for electromagnetic-based hyperthermic therapies," *Sensors (Switzerland)*, vol. 20, no. 10, pp. 1–14, 2020, doi: 10.3390/s20103004.

[32] M. H. H. Tehrani *et al.*, "Use of microwave ablation for thermal treatment of solid tumors with different shapes and sizes-A computational approach," *PLoS One*, vol. 15, no. 6 June, pp. 1–20, 2020, doi: 10.1371/journal.pone.0233219.

[33] S. A. Prahl, "Everything I think you should know about inverse adding-doubling," *Oregon Medical Laser Center, St. Vincent Hospital*, 2011. http://omlc.ogi.edu/software/iad.

[34] B. K. Park *et al.*, "Thermal conductivity of biological cells at cellular level and correlation with disease state," *J. Appl. Phys.*, vol. 119, no. 22, 2016, doi: 10.1063/1.4953679.

[35] Y. Yuan *et al.*, "A heterogeneous human tissue mimicking phantom for RF heating and MRI thermal monitoring verification," *Phys Med Biol.*, vol. 57, no. 7, pp. 2021–2037, 2010, doi: 10.1088/0031-9155/57/7/2021.A.

[36] Y. Yamada, H. Suzuki, and Y. Yamashita, "Time-domain near-infrared spectroscopy and imaging: A review," *Applied Sciences (Switzerland)*, vol. 9, no. 6. MDPI AG, p. 1127, Mar. 17, 2019, doi: 10.3390/app9061127.

[37] D. Grosenick, H. Rinneberg, R. Cubeddu, and P. Taroni, "Review of optical breast imaging and spectroscopy," *J. Biomed. Opt.*, vol. 21, no. 9, p. 091311, 2016, doi: 10.1117/1.jbo.21.9.091311.